ADVANCED MATERIALS
www.advmat.de

Neuron-Inspired Ferroelectric Bioelectronics for Adaptive Biointerfacing

Fang Wang, Lulu Wang, Xule Zhu, Yi Lu, and Xuemin Du**

Implantable bioelectronics, which are essential to neuroscience studies, neurological disorder treatment, and brain–machine interfaces, have become indispensable communication bridges between biological systems and the external world through sensing, monitoring, or manipulating bioelectrical signals. However, conventional implantable bioelectronic devices face key challenges in adaptive interfacing with neural tissues due to their lack of neuron-preferred properties and neuron-similar behaviors. Here, innovative neuron-inspired ferroelectric bioelectronics (FerroE) are reported that consists of biocompatible polydopamine-modified barium titanate nanoparticles, ferroelectric poly(vinylidene fluoride-*co*-trifluoroethylene) copolymer, and cellular-scale micropyramid array structures, imparting adaptive interfacing with neural systems. These FerroE not only achieve neuron-preferred flexible and topographical properties, but also offer neuron-similar behaviors including highly efficient and stable light-induced polarization change, superior capability of producing electric signals, and seamless integration and adaptive communication with neurons. Moreover, the FerroE allows for adaptive interfacing with both peripheral and central neural networks of mice, enabling regulation of their heart rate and motion behavior in a wireless, non-genetic, and non-contact manner. Notably, the FerroE demonstrates unprecedented structural and functional stability and negligible immune response even after 3 months of implantation in vivo. Such bioinspired FerroE are opening new opportunities for next-generation brain–machine interfaces, tissue engineering materials, and biomedical devices.

1. Introduction

Bioelectronics have become an indispensable communication bridge across the biological systems to the external world through sensing, monitoring, or manipulating bioelectrical signals, which are essential to biomedical diagnostics, neurological disorder treatment, and brain–machine interfaces.[1–13] Conventional bioelectronic devices made of metal or silicon are intrinsically rigid and planar, whereas neural tissues are soft and curved.[11,13,14] These significant mechanical and structural dissimilarities lead to severe foreign-body responses, glial encapsulation surrounding the devices, and subsequent electrophysiological signal degradation or loss, especially in chronically implanted neuromodulation scenarios.[13,15–18] Recently, various neuron-like and neural-tissue-like bioelectronic devices have been developed to blur these dissimilarities by mimicking the mechanical, structural, and biochemical properties of neural tissues.[19–24] Despite extensive progress, interface mismatch still exists due to the intrinsic properties of constituent materials, severely hindering their electronic functionality and long-term reliability for integration and communication with neural tissues.[12,25–27] Emerging bioelectronics relying exclusively on polymers, such as photovoltaic polymers and conductive hydrogels, have further narrowed the mechanical and structural disparities between bioelectronics and neural tissues benefiting from their inherent flexibility and tailorable structures.[27–33] However, these polymer-based bioelectronics suffer from grand chemical and functional stability issues due to their sensitivity to complex physiological conditions, hindering their chronically adaptive interfacing with neural tissues.[25,34,35] Aside from the abovementioned issues, current bioelectronics still lack neuron-similar behaviors, such as polarization change-induced bioelectrical signals and formation of high-density neuronal networks (**Figure 1A**).[9,34,36,37] These behaviors are crucial to both Peripheral Nervous System (PNS) and Central Nervous System (CNS) modulation including regulating organ functions[38–40] and treating various neurological disorders,[41,42] whose ongoing development has the potential to revolutionize the strategies to psychological and neurological disorders. Therefore, it is desirable to develop new neuron-like interface materials and bioelectronics that integrate these

F. Wang, X. Zhu, X. Du
State Key Laboratory of Biomedical Imaging Science and System
Center for Intelligent Biomedical Materials and Devices (IBMD)
Shenzhen Institutes of Advanced Technology (SIAT)
Chinese Academy of Sciences (CAS)
Shenzhen 518055, P. R. China
E-mail: xm.du@siat.ac.cn

L. Wang, Y. Lu
State Key Laboratory of Brain Cognition and Brain-inspired Intelligence Technology, Shenzhen Institutes of Advanced Technology (SIAT), Chinese Academy of Sciences (CAS)
Shenzhen-Hong Kong Institute of Brain Science
Shenzhen 518055, P. R. China
E-mail: luyi@siat.ac.cn

F. Wang
College of Physical Science and Technology
Yangzhou University
Yangzhou 225002, P. R. China

The ORCID identification number(s) for the author(s) of this article can be found under https://doi.org/10.1002/adma.202416698

DOI: 10.1002/adma.202416698

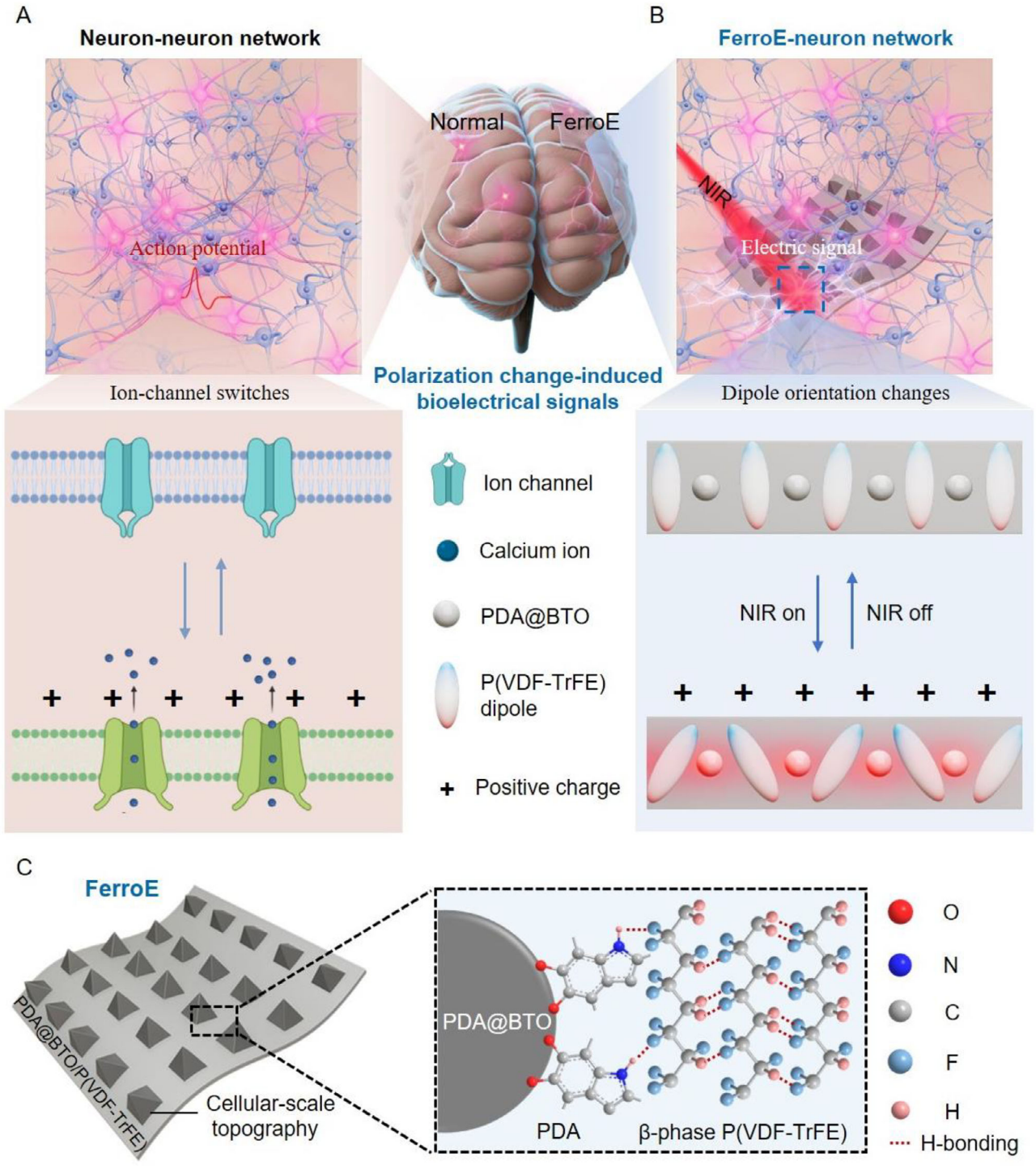

Figure 1. Conceptual scheme of neuron-inspired FerroE. A) Schematic illustration of neuron behaviors including polarization change-induced action potential, and formation of high-density neuronal networks. B,C) Neuron-inspired design of FerroE, incorporating biocompatible PDA@BTO, ferroelectric P(VDF-TrFE) copolymer, and cellular-scale micropyramid array structure for adaptive interfacing.

neuron-preferred properties and neuron-similar behaviors for adaptive interfacing with neural tissues, yet this remains a great challenge.[12,13,17]

Here, we report novel ferroelectric bioelectronics (FerroE) that integrate neuron-preferred flexible and topographical properties and neuron-similar behaviors (i.e., polarization change-induced bioelectrical signals and formation of high-density neuronal networks), imparting seamless integration and adaptive communication with neural systems (Figure 1B). The FerroE consists of three core elements (Figure 1C): biocompatible

polydopamine-modified barium titanate nanoparticles (PDA@BTO) for efficient photo-to-thermal conversion and enhanced ferroelectric performance; ferroelectric poly(vinylidene fluoride-*co*-trifluoroethylene) (P(VDF-TrFE)) copolymer for producing real-time electric signals through reversible polarization changes; and cellular-scale micropyramid array structures to facilitate neuronal adhesion, neurite outgrowth and interconnection. Leveraging on their synergetic interactions, the FerroE not only demonstrate excellent flexibility, uniform topographical structures, highly efficient and stable light-induced polarization changes, and superior capability of producing electric signals (producing ≈3.6 V in 100 milliseconds; no decay after ≈10 000 cycles or 180 days under a physiological condition), but also enable seamless integration and adaptive communication with neuronal networks. Moreover, the FerroE further allow for adaptive interfacing with both peripheral (vagus nerve) and central (motor cortex) neural networks of mice, enabling regulation of their heart rate and motion behavior in a wireless, non-genetic, and non-contact manner. Note that the FerroE demonstrates a superior functionally stable and biocompatible interface with neurons after 3 months of implantation in vivo. By integrating neuron-preferred properties and neuron-similar behaviors, these neuron-inspired FerroE open new directions for next-generation neural interface materials and devices, which may inspire future adaptive capabilities of brain-machine interfaces, tissue engineering materials, and biomedical devices.

2. Results

2.1. Design of Ferroelectric Bioelectronics

To achieve neuron-inspired FerroE, we first synthesized PDA-modified BTO particles (Figure S1, Supporting Information), then dispersed them into a pre-prepared solution of P(VDF-TrFE), and subsequently cast it into a pre-made silicon mold with an inverse micropyramid array for complete solidification and finally high electric field-enhanced polarization (see Experimental Section). The FerroE can be facilely fabricated into a large size of 6-inch diameter, which displays excellent mechanical flexibility and stability as evidenced by optical image and mechanical test (**Figure 2A**; Figures S2 and S3, Supporting Information). The polarization-electric field (P–E) hysteresis curves demonstrate the unique ferroelectricity of the FerroE (Figure S4A, Supporting Information), while the differential scanning calorimetry (DSC) shows that the Curie temperature (T_C) of the FerroE is typically bimodal at 107.8 and 110.7 °C, thus implying stable electrical properties at physiological temperature (Figure S4B, Supporting Information).[43] Scanning electron microscopy (SEM) shows the uniform topographic structure on the FerroE surface, where the rationally designed micropyramid space (size: 5 μm × 5 μm × 3.5 μm, spacing: 5 μm) exhibits similar sizes to that of neuron soma, respectively. Energy-dispersive X-ray spectroscopy (EDS) shows a good dispersion of PDA@BTO within P(VDF-TrFE) due to the intermolecular interactions between the positively charged amine (-NH_2) groups of PDA and negatively charged difluoromethylene (-CF_2) groups of P(VDF-TrFE) (Figure 2B). Atomic force microscopy-infrared (AFM-IR) spectroscopy demonstrates that such intermolecular interactions further promote the β-phase formation of P(VDF-TrFE) (Figure 1C; Figure S5, Supporting Information).[44–46] Notably, the FerroE (5 wt% PDA@BTO/P(VDF-TrFE)) exhibits high β-phase content and d_{33} value that is close to the P(VDF-TrFE) film, suggesting its outstanding electrical properties (Figure S6, Supporting Information).

We further investigate the neuron-similar reversible polarization change behavior of the FerroE. Although the PDA@BTO particles display a broadband absorption range spanning from 200 to 1500 nm (Figure S1C, Supporting Information), 808-nm NIR irradiation is employed for the following experiments based on overall consideration of both relatively strong absorption and superior tissue penetration depths compared to other wavelengths, a critical factor for biomedical applications. Upon exposure to NIR light irradiation, the embedded PDA@BTO particles efficiently convert the absorbed light into in situ temperature rise (Figure S7, Supporting Information), thus decreasing the polarization of the FerroE due to the orientation loss of P(VDF-TrFE) dipoles. Turning off the NIR light irradiation, the reduced temperature leads to a rapid increase of the FerroE polarization owing to the orientation recovery of P(VDF-TrFE) dipoles (Figure 1B). Unprecedentedly, such light-induced dipole orientation alterations triggering the polarization changes of the FerroE further produce electric signals (Figure S8, Supporting Information), behaving similarly to the ion channels' switching-induced polarization change and subsequent action potential generation (80–100 mV) in neurons (Figure 1A).[47] As shown in Figure 2C,D, the FerroE (5 wt% PDA@BTO/P(VDF-TrFE)) can produce ≈3.6 V peak-to-peak open-circuit voltage within 100 milliseconds, which is higher than that of other particle-blended P(VDF-TrFE) films owing to the enhanced ferroelectric performances from PDA@BTO nanoparticles (Figure S9, Supporting Information).[48–50] Moreover, the FerroE demonstrates a unique high voltage yet low current, which can be facilely tuned by varying the PDA@BTO concentration and laser intensity as shown in Figure 2E and Figure S10 (Supporting Information). Note that the reversible polarization alteration behavior of the FerroE shows no evident decay even under 2000-cycle bending, 10 000-cycle impulse NIR irradiation, or even immersed in a cell culture medium at 37 °C for 180 days (Figure S3B, Supporting Information; Figure 2F,G). In addition, the light-induced maximum temperature variation can be constrained within ≈0.5 °C with carefully controlled NIR irradiation conditions (power density of 28 mW mm^{-2}, 10% duty ratio, and 1 Hz), which can eliminate photothermal effects on the neural activities (Figure 2H; Figures S11 and S12, Supporting Information). These results suggest that the FerroE not only achieves neuron-preferred flexible and topographical properties but also enables neuron-similar polarization change-induced bioelectric signals, which are anticipated for adaptive interfacing with neurons.

2.2. Seamless Integration with Neurons

We next investigate if the FerroE can seamlessly integrate with neurons to form high-density neuronal networks similar to natural neurons. First, the poled FerroE sample (FerroE), non-poled FerroE sample (N-FerroE), non-poled flat sample (N-Flat), and non-poled sample (with different surface microstructures or sizes) surfaces are treated with poly-D-lysine (PDL),

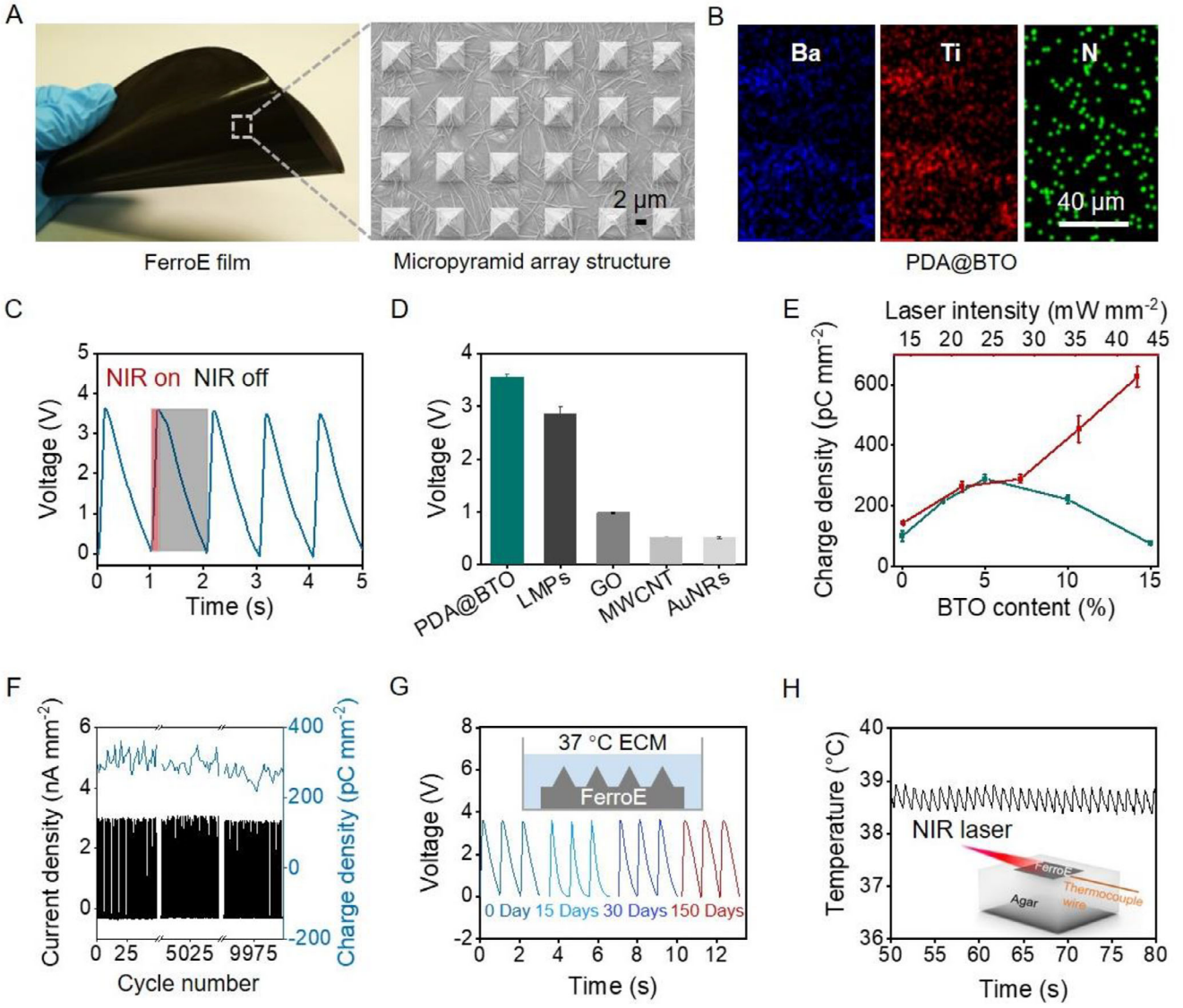

Figure 2. FerroE design. A) Photograph of a 6-inch FerroE film, SEM image of the FerroE surface with micropyramid array structure. B) EDS images of Ba, Ti, N in the FerroE. C) The open-circuit voltage generated by the FerroE under exposure to near-infrared (NIR, 808 nm) irradiation with a power density of 28 mW cm^{-2}, 10% duty ratio, and 1 Hz. D) Comparison of open-circuit voltage generated by P(VDF-TrFE)-based films blended with different photothermal agents, i.e., 5 wt% PDA@BTO, 5% liquid metal particles (LMPs), 0.5% graphene oxide (GO), 1% multiwalled carbon nanotubes (MWCNT), and 20 nM gold nanorods (AuNRs). E) The charge density generated by the FerroE with various concentrations of PDA@BTO nanoparticles or under NIR irradiation with different laser intensities. F) The durability of light-induced reversible polarization changes of the FerroE after 10 000 cycles of pulsed NIR irradiation with a power density of 28 mW cm^{-2}, 10% duty ratio, and 1 Hz. G) The open-circuit voltage generated by the FerroE after immersion in 37 °C cell culture medium for 0, 15, 30, and 180 days under exposure to NIR irradiation with a power density of 28 mW cm^{-2}, 10% duty ratio, and 1 Hz. H) Temperature change in the near-physiological environment, where the FerroE and agar were immersed in the 37 °C water bath and then exposed to NIR irradiation with a power density of 28 mW cm^{-2}, 10% duty ratio, and 1 Hz. The inset schematically illustrates the temperature measurement using a thermocouple placed between the FerroE and agar. All data are presented as mean ± standard deviation (mean ± SD).

respectively. Second, primary cortical neurons obtained from neonatal mice are incubated on these sample surfaces for 9 days, and then the neuron adhesion and morphologies on these surfaces are recorded and compared. As shown in **Figure** 3A–C and Figure S13 (Supporting Information), the fluorescence intensity of vinculin expression on both FerroE and N-FerroE samples is ≈2.4 times higher than that of N-Flat samples, indicating stronger focal adhesion of neurons on the micropyramid array surfaces. Consistent with vinculin expression, the neurons exhibit unprecedentedly high density and interconnection on the FerroE and N-FerroE samples, where somas are located at the micropyramid spaces and the neurites extend and crisscross along the microstructures as evidenced by the SEM and fluorescence images (Figure 3D,E; Figures S14 and S15, Supporting Information). On the contrary, the neurons on the flat samples and samples with different surface microstructures or sizes display fewer neurite outgrowth, thus forming low-density interneural connections (Figure 3F,G; Figure S15A,B,

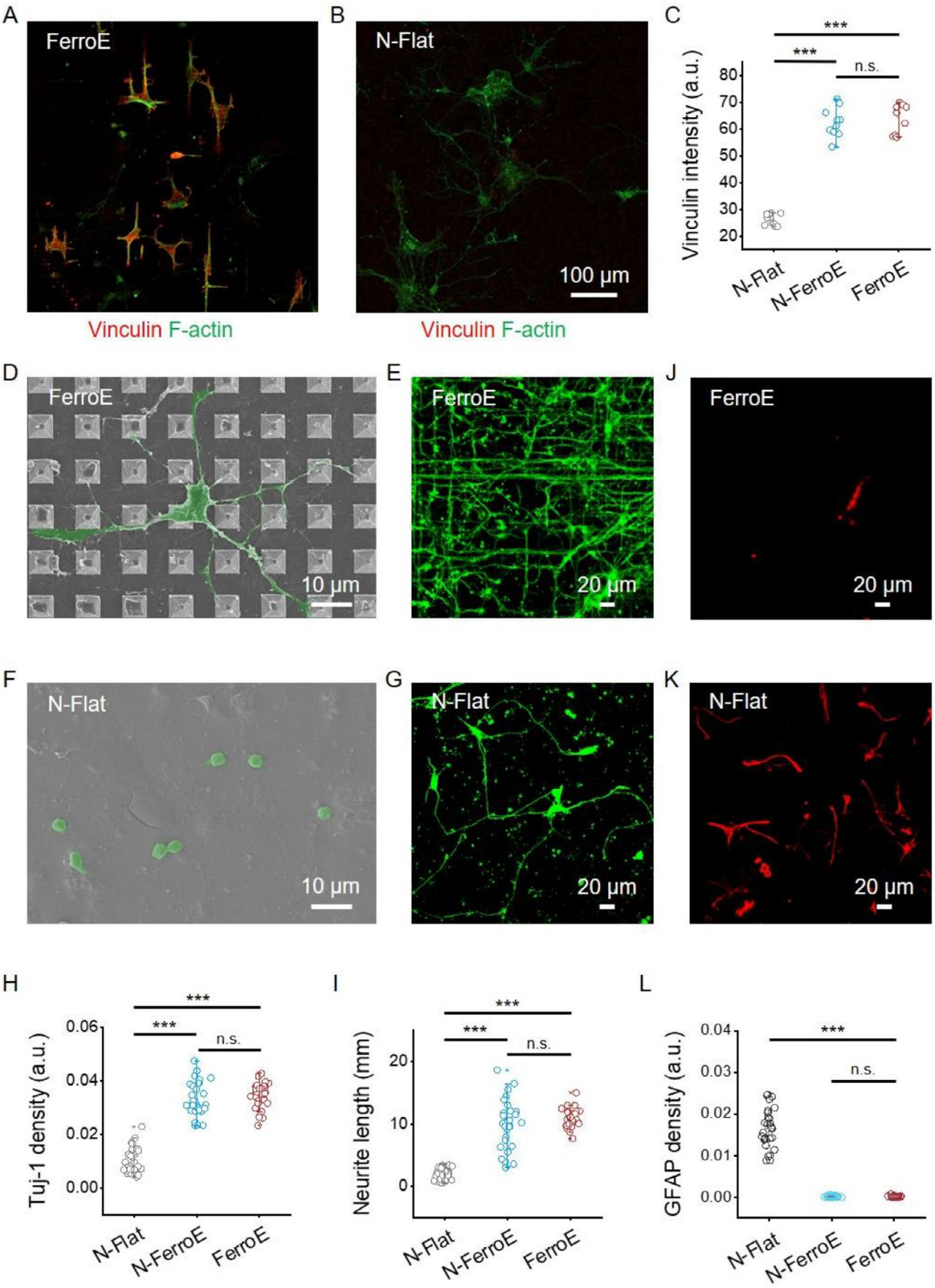

Figure 3. Seamless integration. A,B) Representative fluorescence images showing the vinculin and actin filament (F-actin) of primary cortical neurons cultured on the FerroE and N-FerroE, respectively. C) Quantitative comparisons of vinculin intensity of primary cortical neurons cultured on the N-Flat, N-FerroE and FerroE. n = 10 cells; ***$p < 0.005$; no significance (n.s.) $p > 0.05$, t-test. N-Flat versus N-FerroE: $p = 1.29\times10^{-13}$ (***); N-Flat versus FerroE: $p = 4.04\times10^{-14}$ (***); N-FerroE versus FerroE: p = 0.44 (n.s.); D) SEM image of primary cortical neurons cultured on the FerroE.

Supporting Information). Correspondingly, the class III β-tubulin (Tuj-1, green) expression and neurite length on the FerroE and N-FerroE samples are significantly higher than that of N-Flat samples and samples with different surface microstructures or sizes (Figure 3H,I; Figure S15D,E, Supporting Information), suggesting that the cellular-scale topography promotes their attachment and neurite outgrowth. Furthermore, the neuron-inspired FerroE surfaces demonstrate a general affinity with differentiated rat pheochromocytoma (PC12) cells that have neurogenic characteristics (Figure S16, Supporting Information). These observations indicate that the FerroE with neuron-preferred lysine sequences and topographical features promote unprecedented neuronal adhesion, neurite outgrowth, and interconnection, opening new avenues for next-generation tissue engineering materials and brain-machine interfaces.

We further investigate whether the neuron-inspired FerroE can resist the adhesion of astrocytes, which play an important role in forming glial encapsulation around the implanted bioelectronic devices.[15] Thus, we analyze and compare the astrocyte morphologies and the glial fibrillary acidic protein (GFAP, red) expression on the flat samples and FerroE samples via immunochemical staining (Figure 3J,K). As shown in Figure 3J, unlike the abovementioned high-density interconnected neuronal networks, few astrocytes adhere to the FerroE samples, ascribing to the size mismatch between the astrocyte and the rationally designed micropyramid array. By comparison, a large number of astrocytes adhere to the flat control sample, and display large cell domains (Figure 3K). These observations are further clarified by the GAFP intensity. As shown in Figure 3L, the GAFP intensity on the FerroE sample is negligible, while the intensity on the flat sample is very high. Although similar results can also be observed on the samples with different surface microstructures or sizes, their glia-resistant effect is poorer than that of the FerroE (Figure S15C,F, Supporting Information). Collectively, these results suggest that the neuron-inspired FerroE not only enables the formation and seamless integration with high-density neuronal networks but also exhibits an unprecedented glia-resistant effect, which is essential for safe and reliable interface communication.[16,20,51]

2.3. Adaptive Communication with Neurons

To investigate the interface communication, we further perform intercellular calcium (Ca^{2+}) imaging of HEK293T cells on the FerroE surfaces (**Figure** 4A). HEK293T cells were first cultured on the FerroE and N-FerroE samples respectively for 4 days, then infected with lentivirus containing GCaMP6s, and finally exposed to NIR irradiation (808 nm, 28 mW mm^{-2}, 10% duty ratio, and 1 Hz). As shown in Figure 4B–D, the fluorescence intensity of HEK293T cells on the FerroE surface shows a sharp increase under exposure to NIR irradiation, indicating that the cell depolarization is induced by the polarization/depolarization of the FerroE. Conversely, for HEK293T cells on the N-FerroE surface, the fluorescence shows negligible fluctuations before and after exposure to NIR irradiation. These results suggest that the cell excitation is evoked by the electric signals produced by the polarization changes of the FerroE other than the photothermal effect. Furthermore, we examine the electrophysiological responses of neurons on the FerroE using whole-cell patch-clamp recording (Figure 4E). When exposed to NIR irradiation (28 mW mm^{-2}, 10% duty ratio, and 1 Hz), the FerroE decreases polarization and elicits fast increases of cell membrane potential, leading to neuron depolarization (Figure 4F). By comparison, the N-FerroE without polarization change cannot induce cell membrane potential alteration even under NIR irradiation (28 mW mm^{-2}, 10% duty ratio, and 1 Hz) (Figure 4G). This FerroE-induced high voltage yet low current effect for evoking cell excitation is distinct from previous works that depend on low voltage but high current, where the generated ROS in the FerroE is ≈6 times lower than that of semiconductive p-n Si film (Figure S17, Supporting Information).[52–55] Accordingly, the cell depolarization is primarily induced by photocapacitive effect produced by the polarization changes of the FerroE (Figure 4A), which is different from that of other light-sensitive materials.[55–57] Such unique polarization transmission between the FerroE and the cells decreases the redox reactions that can induce cellular damage. Therefore, the cells still maintain high activity even after exposure to NIR irradiation as evidenced by Figure S18 (Supporting Information). These results indicate that the safe and effective interface communication between the FerroE and cells is similar to that of neuron-neuron communication, affording potential opportunities for modulating in vivo neural systems.

In vitro experiments demonstrate that FerroE can enhance the activity of cells cultured at the interface, providing preliminary evidence for its feasibility in regulating neural activity. We further perform in vivo experiments to evaluate whether the FerroE can modulate the activities of peripheral nerves and induce physiological changes in animals (Figure 3H), for example, heart rate, because tachycardia, marked by an abnormally rapid heart rate, poses several risks, such as increased cardiac workload, arrhythmias, and a heightened risk of stroke. To explore this, we attached the FerroE to the vagus nerve to observe whether it can activate the nerve and subsequently affect the heart rate. As shown in Figure 3I, a customized FerroE-based flexible film is attached onto the left vagus nerve fiber of a mouse, a laser beam (808 nm) delivered by a 200-μm-diameter optical fiber is illuminated on the FerroE, and a pulse oximeter is used to record the mouse's heart rate. Before exposure to NIR irradiation, the anesthetized mouse's heart rate remains at 440 bpm steadily, while the heart

E) Representative fluorescence image of primary cortical neurons cultured on the FerroE. F) SEM image of primary cortical neurons cultured on the N-Flat. G) Representative fluorescence image of primary cortical neurons cultured on the N-Flat. H,I) Quantitative comparisons of Tuj-1 intensity and neurite length of primary cortical neurons cultured on the N-Flat, N-FerroE and FerroE, respectively. $n = 28$ images from 4 samples; ***$p < 0.005$; n.s. $p > 0.05$, *t*-test. H, N-Flat versus N-FerroE: $p = 4.74\times10^{-21}$ (***); N-Flat versus FerroE: $p = 7.63\times10^{-26}$ (***); N-FerroE versus FerroE: p = 0.39 (n.s.); I) N-Flat versus N-FerroE: $p = 2.01\times10^{-14}$ (***); N-Flat versus FerroE: $p = 6.10\times10^{-33}$ (***); N-FerroE versus FerroE: p = 0.19 (n.s.). J,K) Fluorescence images of astrocytes cultured on the FerroE and N-Flat samples. L) Quantitative comparisons of the GFAP density of astrocytes cultured on the N-Flat, N-FerroE and FerroE. $n = 28$ images from 4 samples; ***$p < 0.005$; no significance (n.s.) $p > 0.05$, t-test. N-Flat versus N-FerroE: $p = 5.62\times10^{-25}$ (***); N-Flat versus FerroE: 5.64×10^{-25} (***); N-FerroE versus FerroE: p = 0.98 (n.s.). All data are presented as mean ± SD.

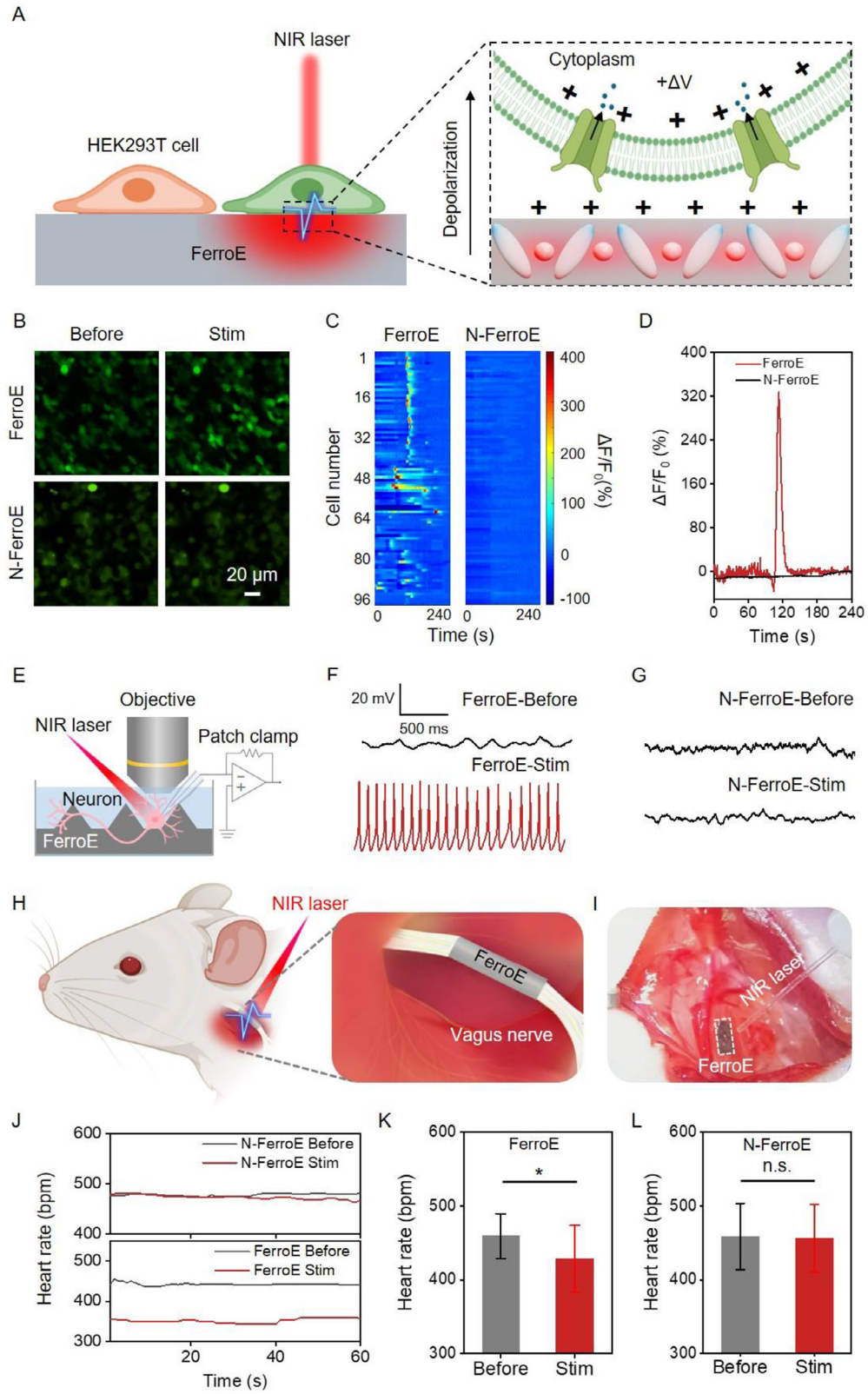

Figure 4. Adaptive communication. A) Schematic of adaptive communication of the FerroE with neurons. The polarization changes of the FerroE under NIR irradiation elicits the depolarization of neuronal membrane potential, subsequently leading to cellular excitation. B) Fluorescence images of GCaMP6s-expressed HEKT293 cells cultured on the N-FerroE and FerroE before and during NIR light irradiation. C) Normalized fluorescence changes ($\Delta F/F_0$) of each GCaMP6s-expressed HEKT293 cell cultured on the N-FerroE and FerroE under NIR irradiation (on at 0 s). D) Representative calcium

rate of the mice rapidly reduces to 360 bpm after exposing the FerroE to NIR irradiation (Figure 4J,K). Conversely, the heart rate of the control mice shows negligible change before and after exposing to the N-FerroE to NIR irradiation (Figure 4L). These results imply that the FerroE not only enables communication with neurons but also imparts a wireless and non-genetic strategy for modulating PNS in vivo, offering a theoretical foundation and the technical feasibility for the clinical treatment of physiological disorders.[38–40]

2.4. Cortical Neural Modulation In Vivo

Besides regulating PNS, we further apply the FerroE for cortical neural modulation in CNS. As shown in **Figure 5**A, and Figure S19A (Supporting Information), a tailored FerroE-based flexible film (2 mm × 2 mm) is attached to the cortex of a mouse brain, a laser beam (808 nm) delivered by a 200-µm-diameter optical fiber is illuminated on the FerroE, and a customized microelectrode array inserts underneath the FerroE to record the brain neural activities. Figure 5B and Figure S19B (Supporting Information) show that the spectrograms of local field potentials (LFPs) that represent spontaneous and stimulated neural activity patterns are recorded in the mice cortex before and under exposure to NIR irradiation. These spectrograms demonstrate that the neuron activities significantly increase when the FerroE is exposed to NIR irradiation. On the contrary, illuminations imposed on the N-FerroE and sample-free cortex show no distinct influences on brain neural activities (Figure S19C–H, Supporting Information). The statistical data further indicate that the neural activities are significantly enhanced by the FerroE under NIR irradiation, as compared with the control samples (Figure 5C). These results reveal that the FerroE are capable of communicating with neural networks in vivo based on photo-induced electric fields, rather than the photothermal effect.

We further investigate whether the FerroE-elicited neural activities of the motor cortex can trigger changes in mouse movement. As shown in Figure 5D and Figure S20 (Supporting Information), an awake and freely-moving mouse with the FerroE attached to the motor cortex (right M1) is placed on an air-supported free-floating Styrofoam ball, and the mouse's movement trajectories are recorded in real-time. Before NIR irradiation, the mouse travels a long distance with continuous trajectories. When the FerroE is illuminated by NIR light, the mice's movement direction shifts distinctly toward the left, along with a sharp decrease in the moving distance (Movie S1, Supporting Information). To quantify the movements, we measured the angle of the leftward deviation of the mice during NIR irradiation. By comparison, the angle of the leftward deviation increases significantly, concomitant with a noticeable reduction in the traveled distance (Figure 5E,F). These observations indicate that the FerroE-evoked neural activities of the motor cortex allow for regulating the movements of mice, which are consistent with the functional organization of the motor control system.

In addition, we further investigate the chronic stability and biosafety of the FerroE in vivo. Figure S21A–D (Supporting Information) show that the FerroE demonstrates complete topographic structures, where the micropyramid size and space remain intact even after being implanted in the mice's brain for 3 months. Benefiting from their superior chemical stability, the FerroE also shows remarkable stability in the polarization variation-induced electrical signal capability as evidenced by the scanning Kelvin probe microscopy (SKPM) images (Figure S22, Supporting Information), which is otherwise impossible in previous works.[34,53,58] Additionally, the atomic force microscopy (AFM) mapping demonstrates that the elastic modulus of the 3-month post-implantation FerroE remains within the same range as the unimplanted control, indicating that the material exhibits exceptional mechanical stability under physiological conditions (Figure S23, Supporting Information). Moreover, the FerroE also exhibits low chronic inflammation after 3 months of implantation in vivo. Figure 5G and Figure S24 (Supporting Information) show the brain slice with sham surgery and the implanted FerroE in the same mouse brain, where the astrocytes are marked using glial fibrillary acidic protein (GFAP), the neurons are labeled using neuronal nuclei (NeuN), macrophages are marked using CD68, and microglia are labeled using Ionized calcium binding adapter molecule 1 (iba1). It is worth noting that the fluorescence intensity of GFAP, NeuN, CD68, and iba1 shows no significant differences between the FerroE site and the sham surgery group, indicating that FerroE elicits a negligible immune response (Figure 5H–J; Figure S24, Supporting Information).

3. Conclusion

In summary, we report novel neuron-like interface materials and bioelectronics (i.e., FerroE) that integrate neuron-preferred flexible & topographical properties and neuron-similar behaviors in one system, enabling unprecedentedly seamless integration and adaptive communication with neural systems. In contrast to other electrophysiology bioelectronics, the FerroE exhibit excellent flexibility, uniform topographical structures, highly efficient and stable light-induced reversible polarization changes, and superior capability of producing electric signals (producing ≈3.6 V in 100 milliseconds; no decay after ≈10 000 cycles or 180 days under a physiological condition), and seamless integration and adaptive communication with neuronal networks. Furthermore, these FerroE allow for intimate interfacing with both peripheral (vagus nerve) and central (motor cortex) neural networks of mice, enabling regulation of their heart rate and motion behavior in a wireless, non-genetic, and non-contact manner. Moreover, the FerroE demonstrate superior structural & functional stability and negligible immune response even after 3 months of implantation

signal traces of cell cultured on the N-FerroE and FerroE. E) Schematically illustrating the whole-cell patch-clamp recording of primary cortical neurons on the FerroE. F,G) Representative traces of cell membrane potential of primary cortical neurons elicited by the FerroE and N-FerroE before and during NIR light irradiation. H) Experimental schematic of vagus nerve stimulation. I) Photographs of vagus nerve stimulation. J) Changes of heart rate of mice treated with FerroE or N-FerroE before and during NIR light irradiation. K,L) Comparison of average heart rates of mice treated with FerroE or N-FerroE before and during NIR light irradiation. FerroE, $n = 6$; N-FerroE, $n = 5$; * $p < 0.05$; n.s. $p > 0.05$, t-test. K, Before versus Stim: $p = 0.04$ (*); L) Before versus Stim: $p = 0.30$ (n.s.). The data in K and L are presented as mean ± SD.

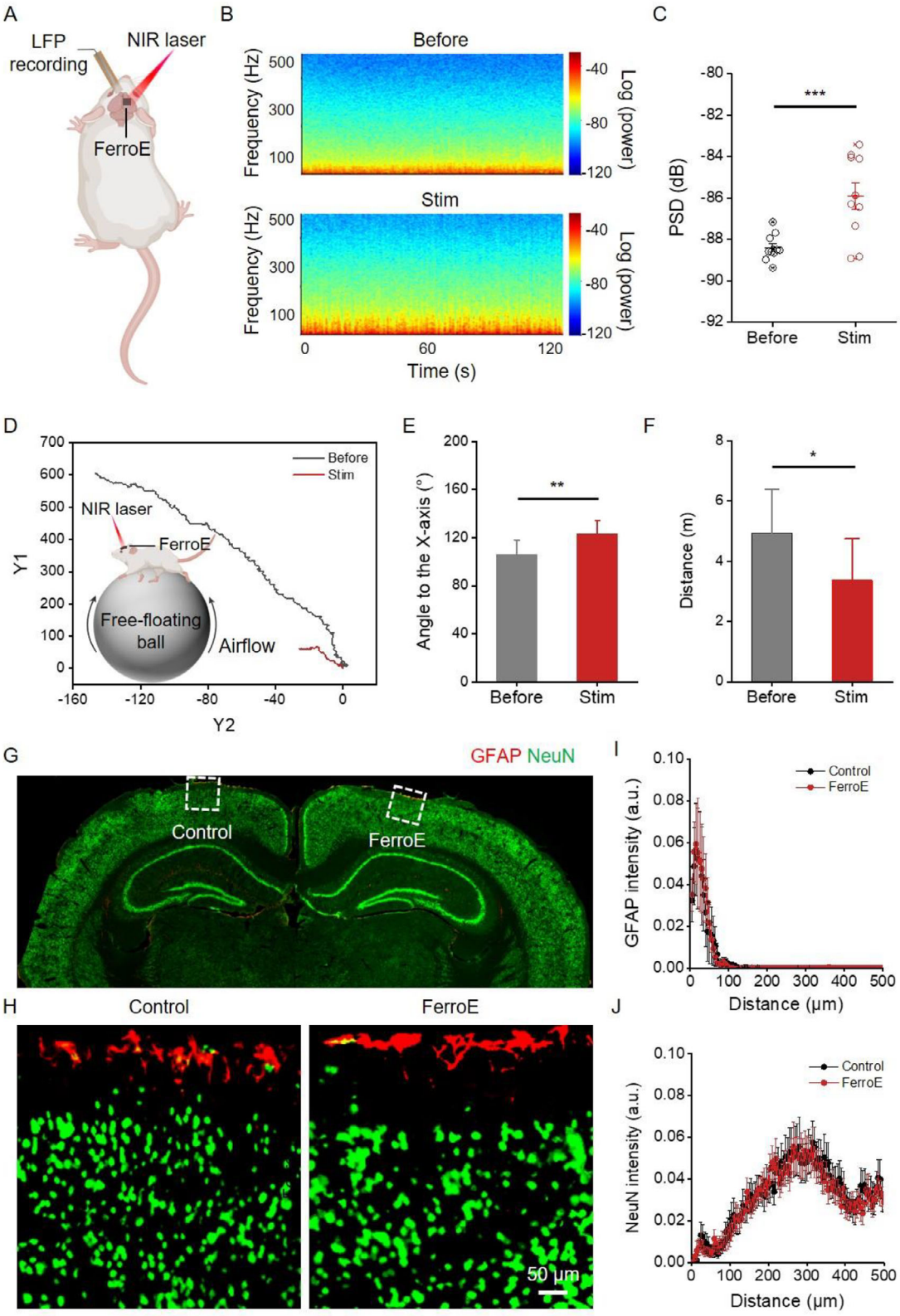

Figure 5. In vivo neuromodulation. A) The schematic of NIR irradiation-induced stimulation and electrophysiological recording of mice with the FerroE implanted on the cortex. B) Representative LFP spectrograms of the mice with the FerroE implanted on the cortex before and during NIR irradiation. C) The comparison of average power spectra density (PSD) of signals before and during NIR light irradiation of the FerroE. $n = 10$ trials from 5 mice; *** $p < 0.005$, *t*-test. Before versus Stim: $p = 0.002$ (***). D) Movement trajectories of mice before and during NIR light irradiation of the FerroE. The inset

in vivo. Although the current design of the FerroE relies on an external NIR laser source, which limits both photoconversion efficiency and device portability. Such limitations can be addressed by integrating light emitters, such as MicroLEDs, to enhance photoconversion efficiency and improve portability, thereby enabling more practical applications.[59] In addition, the optical stimulation is not inherently selective for specific neurons; however, the high spatial selectivity of the FerroE enables targeted stimulation of neuron populations by dynamically shaping the photoinduced virtual electrodes. This new tool eliminates the need for genetic engineering, thereby avoiding associated ethical and safety concerns.[28] We can envision that these neuron-like interface materials and bioelectronics that possess indistinguishable features from neurons would open new opportunities for next-generation brain-machine interfaces, tissue engineering materials, and biomedical devices.[12,20,60–64]

4. Experimental Section

Materials: Poly(vinylidene fluoride-*co*-trifluoroethylene) (P(VDF-TrFE), 70/30 mol%) with M_w of 520 000–860 000 was purchased from Piezotech (Pierre-Benite, France). Dimethyl sulfoxide (DMSO) was purchased from Aladdin Reagent Co., Ltd (Shanghai, China). Dopamine hydrochloride, tris(hydroxymethyl)aminomethane, Triton-X-100, Poly-D-lysine (PDL), and paraformaldehyde (PFA) were purchased from Sigma–Aldrich (Missouri, USA). Dulbecco's phosphate-buffered saline (PBS, pH: 7.4) was purchased from Gibco (New York, USA). $BaTiO_3$ nanoparticles (BTO, 100 nm, cubic phase) was obtained from Beijing Deke Daojin Science and Technology Co., Ltd (Beijing, China). All reagents were used as purchased without further purification. Ultrapure water (18.2 MΩ·cm) was produced from a water purification system (Arioso Power II, Human, Korea).

Preparation of PDA@BTO Nanoparticles: 0.158 g BTO nanoparticles were first dispersed in 100 mL water under sonicated using ultrasound (KQ5200DE, 200 W) for 0.5 h. 0.12 g tris(hydroxymethyl)aminomethane and 0.2 g dopamine hydrochloride were added in the above suspension. After stirring for 24 h, the suspension was centrifugation at 10 000 rpm for 10 min, and the supernatant was removed. Finally, the collected PDA@BTO nanoparticles dispersed in DMSO with a certain concentration were used in the following experiments.

Preparation of PDA@BTO/P(VDF-TrFE) Composite Films: First, PDA@BTO/P(VDF-TrFE) suspensions were obtained by dissolving P(VDF-TrFE) powders (100 mg mL^{-1}) into the suspension of PDA@BTO nanoparticles in DMSO followed by overnight stirring. Then, the contents of PDA@BTO nanoparticles were adjusted to 0, 2.5, 5, 10, 15 wt% (based on the weight of BTO). Then, 30 mL of the preprepared solution was cast on a silicon wafer or a 6-inch Si mold with inverse micropyramid array (size: 5 μm × 5 μm × 3.5 μm, spacing: 5 μm), and inverse microcylinder arrays (diameter: 3 μm, height: 5 μm, spacing: 5 μm; diameter: 10 μm, height: 10 μm, spacing: 10 μm) fabricated by photolithography and anisotropic chemical wet etching. After dried at 80 °C for 12 h and annealed at 130 °C for 8 h in a vacuum oven, the film was peeled off from the substrates. The resulted films were corona poling with a high voltage of 22 kV for 25 min at 90 °C.

Mechanical Property Measurement: The mechanical characterization of FerroE films was conducted using a universal tensile testing machine (HY-0580, Shanghai Hengyi Testing Instruments Co., Ltd., China). Specifically, FerroE films with pre-determined dimensions (length, width, and thickness) were secured to the two clamps of the universal tensile testing machine. In accordance with the ASTM C1557 standard, tensile tests were carried out at a consistent tensile speed of 1 mm min^{-1}. Strain-stress curves were documented. Subsequently, Young's modulus was examined based on the strain-stress curves derived from a minimum of five independent experiments.

Electrical Property Measurement: In order to measure the electrical properties of the above poled films, 200-nm indium-tin oxide (ITO) electrodes were prepared via sputtering on both sides of the PDA@BTO/P(VDF-TrFE) films at room temperature. The open-circuit voltage and short-circuit current of particle-blended P(VDF-TrFE) films with different contents of PDA@BTO (0, 2.5, 5, 10, 15 wt%), 5% LMPs, 0.5% GO, 1% MWCNT, 20 nM AuNRs[46] were recorded by a digital source meter (Keithley 2470, USA) by irradiation with 808-nm NIR light with various laser power densities of 14, 21, 28, 35, 42 mW mm^{-2} (10% duty ratio and 1 Hz), and different duty cycles of 10, 20, 30, 40, 50% (1 Hz, 28 mW mm^{-2}), respectively.

5 wt% PDA@BTO/P(VDF-TrFE) films immersed with cell culture medium at 37 °C for different time (0, 15, 30 and 180 days) were taken out and dried at room temperature, then sputtered the electrodes and measured the electric property through the same procedures.

For electrical measurement under bending, FerroE with 30 mm in length and 5 mm in width was clamped between two stepper motors with an initial central spacing of 25 mm. The stepper motors were controlled to adjust the displacement, reducing the central spacing to 20, 15, and 10 mm, thereby achieving bending radius of 11, 7.5, and 5.9 mm, respectively. During the reciprocating motion of the stepper motors, the electrical performance of the FerroE was tested under 2000 bending cycles.

Surface Potential Measurements: The stability of electric property of PDA@BTO/P(VDF-TrFE) films was detected by the scanning Kelvin probe microscopy (SKPM). To evaluate the surface potential of the PDA@BTO/P(VDF-TrFE) film before and after 3 months implantation, SKPM (Asylum Research Cypher S, USA) measurements were performed under 808-nm NIR laser irradiation with 5 mW mm^{-2}. The initial surface potential of the composite film keeps approximating zero by partial coating silver paste and grounding. The change of surface potential nearby the grounded area of the PDA@BTO/P(VDF-TrFE) films can be recorded via periodical 808-nm NIR irradiation with interval time of 2.5 min at room temperature.

Temperature Measurement: A simulated physiological tissue consists of a bulk agar immersed into 37 °C water was used to detect the temperature change of the brain tissue under the PDA@BTO/P(VDF-TrFE) film with NIR light irradiation. The temperature changes were measured using a type-K thermocouple with a 0.1 mm bead diameter inserted into the interface of the PDA@BTO/P(VDF-TrFE) film (2 mm × 2 mm) and the agar under NIR light irradiation (1 Hz, 10% duty ratio, 28 mW mm^{-2}) by a data acquisition system (National Instruments, NI cDAQ-9171-9212, USA).

PC12 Cell Culture: PC12 cells, commonly utilized as a neuronal model, were seeded on the surface of N-Flat, N-FerroE and FerroE at a density of 1×10^5 cells per well of 4-well plates, respectively. Prior to seeding, the films underwent a coating process with PDL for 6 h, followed

shows a schematic diagram of the mice on an air-supported free-floating Styrofoam ball with implanted FerroE on the cortex, whose motion functions is modulated by NIR-induced stimulation. E) Angle of leftward deviation of mice before and during NIR light irradiation of the FerroE. $n = 10$ trials from 5 mice; ** $p < 0.01$, *t*-test. Before versus Stim: $p = 0.004$ (**). F) Distance traveled by mice before and during NIR light irradiation of the FerroE. $n = 10$ trials from 5 mice; * $p < 0.05$, *t*-test. Before versus Stim: $p = 0.048$ (*). G,H) Fluorescence images of GFAP and NeuN for the brain tissues of mice in the sham surgery group (left) or being implanted with the FerroE on the cortex (right), red, GFAP; green, NeuN. I,J) Quantitative analysis of GFAP and NeuN between the sham surgery group and the FerroE ($n = 18$ slices from 6 mice), respectively. Quantitative analysis of GFAP and NeuN expression was performed using intensity profiles as a function of the distance from the FerroE interface. All data are presented as mean ± standard error of the mean (mean ± SEM).

by thorough washing with PBS three times. The PC12 cells were cultured at 37 °C under 5% CO_2 in high glucose-Dulbecco's modified Eagle medium (H-DMEM, Gibco), supplemented with 10% fetal bovine serum (FBS, Gibco) and 1% penicillin-streptomycin antibiotic solution (10 000 U·mL^{-1}, Gibco). The culture medium was completely refreshed 4 h post-seeding and subsequently replaced every 2 days to sustain cell proliferation. On the 9th day, the cells were stained with calcein acetoxymethyl ester (calcein-AM, Sigma). Briefly, PC12 cells were washed with PBS and then incubated in RPMI 1640 medium (Gibco) containing 2.5 µM of calcein-AM at 37 °C. Following a 30 min incubation period, the PC12 cells were washed with PBS, and fluorescence images were captured using a fluorescent microscope (Olympus X71, Japan). The acquired images were processed using ImageJ software (National Institutes of Health).

Primary Cell Culture: Prior to initiating primary cell culture, N-Flat, N-FerroE, non-poled samples with different microstructures (3 µm-microcylinder and 10 µm-microcylinder arrays), and FerroE were prepared and coated with PDL at a concentration of 0.1 mg mL^{-1} for a duration of 6 h. The process of isolating and culturing of primary cells adhered to established protocols. In brief, primary cells were obtained from neonatal mice (24-h old, CD1) and cultured in neurobasal media (Thermo Fisher Scientific) supplemented with 2% B27 (Thermo Fisher Scientific) and 1% penicillin-streptomycin (Thermo Fisher Scientific). The cells were then seeded onto the surface of the films at a density of 1×10^5 cells mL^{-1} and maintained in a humified incubator at 37 °C with 5% CO_2. The media were replaced every 24 h to ensure optimal cell growth conditions. Upon reaching 9 days in vitro, the cells were fixed with 4% PFA in PBS for 15 min, permeabilized with 0.5% Triton-X-100 in PBS for 20 min, and subsequently blocked with PBS containing 10% normal goat serum (NGS, Jackson Immuno Research) for 30 min. Immunostaining was performed using the anti-beta III tubulin neuronal marker (Tuj-1, 1:500, Abcam) and anti-glial fibrillary acidic protein (GFAP, 1:1000, Abcam), which was incubated overnight at 4 °C to label neurons. Following PBS washing, the secondary antibody, Alexa fluor 488 goat anti-mouse and Alexa fluor 594 goat anti-rabbit (Jackson Immuno Research, 1:200), were added and incubated for 1 h. The fluorescence images were conducted and captured using a laser scanning confocal microscope (Zeiss LSM900, Germany). Image analysis was carried out using Image J software (National Institutes of Health).

Immunofluorescence for Cells: After 12 days of co-incubation with N-Flat, N-FerroE and FerroE, immunofluorescent staining of primary cell (fixed in 4% PFA, permeabilized with 0.1% Triton X 100). The sections were washed in PBS, blocked with blocking buffer (PBS + 10% normal goat serum) and incubated with primary antibodies (1:50 anti-vinculin, Abcam, ab129002), overnight at 4 °C. The following day, the sections were incubated with secondary antibodies for 6 h (1:1000 AlexaFluor 568, goat anti-rabbit antibody, ab175471). F-actin was labeled using green-fluorescent Alexa Fluor 488 phalloidin (1:100 Cat. no. A12379), and counterstained with DAPI (1:300 Sigma–Aldrich). Finally, they were mounted on slides using antifade reagent (Biosharp, BL701A) and imaged using a laser scanning confocal microscope (LSCM, Zeiss LSM900, Germany). Image analysis was carried out using Image J software (National Institutes of Health).

Calcium Imaging of HEK293T Cells: HEK293T cells, a class of widely utilized cell line known for its high transfection efficiency, were employed in this study for calcium imaging experiment. Briefly, HEK293T cells were cultured on N-FerroE and FerroE with H-DMEM, supplemented with 10% FBS and 1% penicillin-streptomycin antibiotic solution, at 37 °C in a humidified incubator with 5% CO_2. The culture medium was fully replaced 4 h post-seeding and then renewed every 2 days. On the 4th day, HEK293T cells were infected with lentivirus containing GCaMP6s (HEK-GCaMP6s cells). Following a 2-day incubation period, the HEK-GCaMP6s cells were subjected to video recording using a fluorescent microscope (Olympus X71, Japan) with a 30 s baseline followed by 240 s of NIR light stimulation (808 nm, 1 Hz, 10% duty ratio, 28 mW mm^{-2}). The fluorescence images were analyzed using ImageJ software (National Institutes of Health). Normalized fluorescence changes were calculated according to the formula $\Delta F/F_0 = (F-F_0)/F_0$, where F_0 represents the baseline intensity (baseline 10 s).

Viability Test of HEK293T Cell: In vitro biocompatibility of the films was also evaluated using HEK293T cells and cell viability assay kits. HEK293T cells (1×10^5) were seeded onto the films in 24-well plates and incubated in H-DMEM with 10% FBS and 1% penicillin-streptomycin antibiotic solution. The cultures were kept at 37 °C in a humidified atmosphere with 5% CO_2. After 2 days, cell viability was assessed using Calcein-AM/EthD staining. Fluorescence images of the cells were captured with an Olympus X71 microscope. Live and dead cells were manually counted in all groups using ImageJ software.

Monitoring of Intracellular ROS: PC12 cells were cultured on the FerroE and Si films, then stained with a ROS fluorescent probe, dichlorofluorescein diacetate (DCFDA, Sigma–Aldrich). The dynamics of the intracellular ROS for the PC12 cells were monitored upon exposure to NIR irradiation at 1 Hz, 50% duty ratio, 20 mW mm^{-2}. After incubating the samples with DCFDA according to the manufacturer's protocol, time-lapse recorded fluorescence images of the samples during and after NIR irradiation using the LSCM. We then analyzed the ROS signaling of each cell ($n = 6$ cells) and the average traces of the normalized fluorescence changes ($\Delta F/F_0$) over time, according to representative LSCM images, with the assistance of the ZEN 2 software.

In Vitro Electrophysiological Recording: Primary cortical neurons were perfused with artificial cerebrospinal fluid (ACSF) containing the following: 119 mM NaCl, 2.5 mM KCl, 1.25 mM NaH_2PO_4, 11 mM Glucose, 25 mM $NaHCO_3$, 15 mM HEPES, 1.5 mM $MgSO_4$, 2.5 mM $CaCl_2$ (pH 7.2–7.4) at room temperature. Cells were identified with differential interference contrast optics (DIC; Olympus, BX51WIF). Due to the opaque material, live and dead cell staining (Invitrogen) method was used to record the cells excited by 488 nm laser. Recording pipettes (3–6 MΩ) were pulled with a micropipette puller (MP-500, RWD). For whole-cell recordings, pipettes were filled with internal solution that contained the following: 116 mM K-gluconate, 6 mM KCl, 8 mM NaCl, 0.2 mM EGTA, 2 mM MgATP, 0.3 mM Na_3GTP, and 10 mM HEPES (pH 7.2-7.4). Voltage-clamp recordings were performed with a computer-controlled amplifier (MultiClamp 700B, Molecular Devices) upon exposure to NIR irradiation at 1 Hz, 10% duty ratio, 28 mW mm^{-2}. Recorded traces were low-pass filtered at 3 kHz and sampled at 10 kHz (Digidata 1550B, Molecular Devices). Collected data were analyzed using Clampfit 10 software (Molecular Devices).

Animal: All animal procedures were approved by the Ethics Committee for Animal Research at the Shenzhen Institutes of Advanced Technology, Chinese Academy of Sciences (Approval No. SIAT-IACUC-210113-NS-LY-A1509).

Vagus Nerve Stimulation and Heart Rate (HR) Measurements: Male BALB/C mice aged 6–8 weeks were employed for in vivo experiments. The mice were housed under controlled standard conditions, affording them ad libitum access to both food and water. The housing environment maintained a constant temperature at 24 °C, with a 12 h light/dark cycle and humidity level set at 50%.

BALB/C mice were anaesthetized with isoflurane, followed by placement on a surgical platform to ensure stability and accessibility during the procedure. Subsequently, the left vagus nerve was exposed and the FerroE was positioned on the vagus nerve fiber. The N-FerroE sample was designated to serve as the control group. A 200-µm optical fiber was positioned at a standardized distance of 5 mm from the films to serve as a conduit for delivering near-infrared light pulses (808 nm, 1 Hz, 10% duty ratio, 28 mW mm^{-2}). For HR monitoring in an anesthetized mouse, hair was removed from the mouse's leg skin using a depilation cream (VEET Gel). Subsequently, a sensor was carefully attached to the leg of the mouse to enable the acquisition of HR signals from the carotid arteries. HR measurements were recorded using a pulse oximeter (MouseOx Plus; Starr Life Sciences, USA).

In Vivo Electrophysiological Recording: Following anesthesia induction, a 2 mm × 2 mm hole was carefully drilled through the skull at the cortex region of BALB/C mouse. The FerroE was positioned onto the cortex surface and a customized microelectrode array was delicately inserted below the sample, allowing for detailed neural recording. To further investigate the neural response, a 200-µm optical fiber with a numerical aperture of 0.37 (Thorlabs) was strategically positioned at a distance of 5 mm from the films. This optical fiber served as a conduit for delivering near-infrared

light pulses (808 nm, 1 Hz, 10% duty ratio, 28 mW mm^{-2}). N-FerroE and a sham surgery group (injuries on the cortex) were considered as control group (n = 5 mice per group). Electrophysiological recordings were conducted using a multi-channel neural acquisition processor (Plexon, USA) with a 1 kHz sampling frequency and a bandpass filter set between 1 and 500 Hz. The acquired data were processed and analyzed using custom software developed in MATLAB (MathWorks) and NeuroExplorer (Plexon, USA). To assess the neural response dynamics, power spectra density (PSD) analyses were performed using data collected during the stimulation period (120 s) for each trial.

Behavior Tests: BALB/C mice were anaesthetized with isoflurane and placed in the stereotactic frame. A custom-made metal headplate was attached to the cleaned and dried skull using stainless steel screws and dental cement, ensuring stable fixation and minimizing movement artifacts during subsequent experimental procedures. Then a careful surgical procedure was undertaken to create a 2 mm × 2 mm hole in the skull at the cortex region. The FerroE was fixed onto the cortex surface. Following a recovery period of one-week post-surgery, awake mice were head-fixed using two horizontal bars secured to the headplates with screws, allowing for free movement on an air-supported free-floating Styrofoam ball (Thinkertech, China). Habituation sessions were conducted over a minimum of three days, with mice given the opportunity to freely explore and acclimate to the experimental setup for thirty minutes each session. On the test day, mice were once again head-fixed. An optical fiber, with a diameter of 200 µm, was positioned at a standardized distance of 5 mm from the films, enabling the delivery of NIR light (808 nm, 1 Hz, 10% duty ratio, 28 mW mm^{-2}). Concurrently, the mice's movement trajectories were recorded in real-time, synchronously capturing their behavioral responses to the optical stimuli. To assess behavioral alteration, the angle of leftward deviation and distance analyses were performed using data collected during the stimulation period (60 s) for each trial.

Immunochemical Staining for Brain Slices: The experimental design involved the categorization of FerroE into a test group, whereas a sham surgery group served as control. The mice underwent anesthesia induction with isoflurane, administered at 3% for induction and maintained at 1.5% for the duration of the procedure. Subsequently, the mice were carefully fixed in a standard stereotaxic frame (RWD). A 2 mm × 2 mm hole was carefully drilled through the skull at the cortex regionin each mouse. The FerroE was implanted beneath the skull, specifically over the cortical region of the mice, and fixed with dental cement (without NIR irradiation). After 12 weeks, the mice were anaesthetized, followed by perfusion with PBS to flush out blood. Subsequent perfusion with 4% PFA in PBS facilitated tissue fixation. The brains were removed and post-fixed in 4% PFA at 4 °C overnight, followed by equilibration in a 30% sucrose solution. Horizontal sections (30-µm thick) were obtained using a cryostat microtome (Leica CM1950, Germany). Primary antibodies targeting NeuN (1:500, Millipore), GFAP (1:1000, Abcam), CD68 (1:200, Abcam, ab31630), and Ibal (1:500, Wako, 019–19741) were applied and left to incubate overnight at 4 °C. Subsequent application of secondary antibodies, including Alexa Fluor 488-conjugated goat anti-mouse (Jackson Immuno Research, 1:200) and Alexa Fluor 594-conjugated goat anti-rabbit (Jackson Immuno Research, 1:200), facilitated visualization of the targeted cellular components. The fluorescence images were observed and acquired using an automated slide scanner (Olympus, VS120, Japan). These images served as the basis for quantitative analyses, conducted using custom software developed in MATLAB (MathWorks). Quantitative assessment included the calculation of staining intensities for NeuN, GFAP, CD68 and Iba1 as a function of distance from the implant surface. The average intensity profiles of the analyzed area within a distance of 500 µm from the implant-neural interface are shown.

Characterizations: The light absorption spectrum of PDA@BTO nanoparticles was measured using an UV-vis-near-infrared spectrometer (Shimadzu UV-3600i Plus, Japan). The morphology and elemental maps of PDA@BTO nanoparticles were analyzed by using a transmission electron microscope (TEM, Thermo Fisher Talos F200S G2 with Super-X G2, USA) and an energy-dispersive X-ray spectroscopy (EDS). Differential scanning calorimetry (DSC) thermogram was measured using a Thermal Analysis System (Mettler DSC3, Switzerland), heated from 30 to 130 °C with a temperature increase of 10 °C min^{-1}, under a nitrogen atmosphere. The polarization-electric field (P-E) hysteresis measurements using a ferroelectric analyzer (PK-FERRO20B, USA) at 10 Hz and room temperature. The molecular structures were measured by Fourier transform infrared (FTIR) spectroscopy (Thermo Fisher Scientific Nicolet iS5, USA). The piezoelectric coefficient of the polarization FerroE was measured using a quasistatic d_{33} instrument (ZJ-3AN, China) at room temperature. The PDA@BTO/P(VDF-TrFE) films were analyzed by using a field emission scanning electron microscopy (SEM, Sigma, Carl Zeiss 300, Germany) and EDS (Bruker XFlash 6|60 detector, Germany) to evaluate morphologies and elemental maps. Atomic force microscopy-infrared spectroscopy measurements were implemented using a nano-IR2 (AFM-IR, Anasys Instruments, USA). An Au-coated NIR2 probe (Anasys, PR-EX-TnIR-A-10, USA) with a force constant of 1–7 N m^{-1} and a frequency of ∼75 kHz was used. The used 808-nm NIR laser power density was detected by a Thorlabs PM100D optical power meter equipped with a Thorlabs S425C photodiode sensor (diameter, 25.4 mm; power range, 2 mW–10 W; wavelength range, 190 nm-20 µm). The optical images of PDA@BTO/P(VDF-TrFE) films were photographed by a digital camera (Canon EOS 7D Mark II, Japan). High-resolution thermal images of the PDA@BTO/P(VDF-TrFE) films under NIR irradiation were obtained with an infrared thermometer (R550Pro, 21 µm, NEC, Japan). To evaluate the surface morphologies and potentials of the PDA@BTO/P(VDF-TrFE) films, Scanning Kelvin probe force microscopy (SKPM, Asylum Research Cypher S, USA) was used in this experiment. The elastic modulus mapping of the FerroE before and after 3-month implantation was measured using an AFM (Bruker Dimension Icon, Germany).

Statistical Analysis: Electrical and mechanical properties are expressed as means ± standard deviation (SD) (n = 5) in Figure 2D, E, Figures S2B, S6D, and S21C,D (Supporting Information). The data in Figures 3 and 4, Figures S15 and S16, and S18 (Supporting Information) were shown as mean ± SD. The data in Figure 5 and Figure S24 (Supporting Information) were shown as means ± standard error of mean (SEM). Statistical analysis was performed with OriginPro 2019b. The significance of the data presented was determined by a two-sample t test for Figures 3 and 5I,J, Figures S15, S16, S18, S24 (Supporting Information) and by a paired t test for Figures 4 and 5C,E,F, Figure S19 (Supporting Information). And the threshold for significance was at $p < 0.05$.

Supporting Information

Supporting Information is available from the Wiley Online Library or from the author.

Acknowledgements

The authors acknowledge the financial support provided by Shenzhen Medical Research Fund (B2302045), the National Natural Science Foundation of China (52022102, 52261160380, 32471042, 32300845), the National Key R&D Program of China (2017YFA0701303), the Youth Innovation Promotion Association of CAS (Y2023100), the Fundamental Research Program of Shenzhen (RCJC20221008092729033, JCYJ20220818101800001) and The Guangdong Basic and Applied Basic Research Foundation (2024A1515010645).

Conflict of Interest

The authors declare no conflict of interest.

Author Contributions

F.W. and L.L.W. contributed equally to this work. X.M.D. and Y.L conceived the idea and supervised the study. F.W. and L.L.W. carried out the experiments with assistance from X.L.Z., X.M.D., and Y.L. analyzed the results, and wrote the manuscript with output from F.W. and L.L.W. All authors contributed to the discussion and interpretation of the results.

Data Availability Statement

The data that support the findings of this study are available from the corresponding author upon reasonable request.

Keywords

adaptive biointerface, bioelectronics, ferroelectric materials, neuromodulation, neuron-like

Received: October 30, 2024
Revised: May 14, 2025
Published online:

[1] D.-H. Kim, N. Lu, R. Ma, Y.-S. Kim, R.-H. Kim, S. Wang, J. Wu, S. M. Won, H. Tao, A. Islam, K. J. Yu, T.-I. Kim, R. Chowdhury, M. Ying, L. Xu, M. Li, H.-J. Chung, H. Keum, M. McCormick, P. Liu, Y.-W. Zhang, F. G. Omenetto, Y. Huang, T. Coleman, J. A. Rogers, *Science* **2011**, *333*, 838.
[2] T. Someya, Z. Bao, G. G. Malliaras, *Nature* **2016**, *540*, 379.
[3] J. Li, Y. Liu, L. Yuan, B. Zhang, E. S. Bishop, K. Wang, J. Tang, Y.-Q. Zheng, W. Xu, S. Niu, L. Beker, T. L. Li, G. Chen, M. Diyaolu, A.-L. Thomas, V. Mottini, J. B.-H. Tok, J. C. Y. Dunn, B. Cui, S. P. Paca, Y. Cui, A. Habtezion, X. Chen, Z. Bao, *Nature* **2022**, *606*, 94.
[4] B. Zhang, J. Li, J. Zhou, L. Chow, G. Zhao, Y. Huang, Z. Ma, Q. Zhang, Y. Yang, C. K. Yiu, J. Li, F. Chun, X. Huang, Y. Gao, P. Wu, S. Jia, H. Li, D. Li, Y. Liu, K. Yao, R. Shi, Z. Chen, B. L. Khoo, W. Yang, F. Wang, Z. Zheng, Z. Wang, X. Yu, *Nature* **2024**, *628*, 84.
[5] Y. Ma, Y. Zhang, S. Cai, Z. Han, X. Liu, F. Wang, Y. Cao, Z. Wang, H. Li, Y. Chen, X. Feng, *Adv. Mater.* **2020**, *32*, 1902062.
[6] G. Hong, T.-M. Fu, M. Qiao, R. D. Viveros, X. Yang, T. Zhou, J. M. Lee, H.-G. Park, J. R. Sanes, C. M. Lieber, *Science* **2018**, *360*, 1447.
[7] P. Li, J. Zhang, H. Hayashi, J. Yue, W. Li, C. Yang, C. Sun, J. Shi, J. Huberman-Shlaes, N. Hibino, B. Tian, *Nature* **2024**, *626*, 990.
[8] Z. Liu, Y. Hu, X. Qu, Y. Liu, S. Cheng, Z. Zhang, Y. Shan, R. Luo, S. Weng, H. Li, H. Niu, M. Gu, Y. Yao, B. Shi, N. Wang, W. Hua, Z. Li, Z. L. Wang, *Nat. Commun.* **2024**, *15*, 507.
[9] G. Hong, C. M. Lieber, *Nat. Rev. Neurosci.* **2019**, *20*, 330.
[10] S. R. Patel, C. M. Lieber, *Nat. Biotechnol.* **2019**, *37*, 1007.
[11] S. M. Won, E. Song, J. T. Reeder, J. A. Rogers, *Cell* **2020**, *181*, 115.
[12] E. Song, J. Li, S. M. Won, W. Bai, J. A. Rogers, *Nat. Mater.* **2020**, *19*, 590.
[13] C. Zhao, J. Park, S. E. Root, Z. Bao, *Nat. Rev. Bioeng.* **2024**, *2*, 671.
[14] A. Ahnood, A. Chambers, A. Gelmi, K.-T. Yong, O. Kavehei, *Chem. Soc. Rev.* **2023**, *52*, 1491.
[15] J. W. Salatino, K. A. Ludwig, T. D. Y. Kozai, E. K. Purcell, *Nat. Biomed. Eng.* **2017**, *1*, 862.
[16] R. Chen, A. Canales, P. Anikeeva, *Nat. Rev. Mater.* **2017**, *2*, 16093.
[17] X. Tang, H. Shen, S. Zhao, N. Li, J. Liu, *Nat. Electron.* **2023**, *6*, 109.
[18] J. Yin, S. Wang, T. Tat, J. Chen, *Nat. Rev. Bioeng.* **2024**, *2*, 541.
[19] X. Dai, G. Hong, T. Gao, C. M. Lieber, *Acc. Chem. Res.* **2018**, *51*, 309.
[20] X. Yang, T. Zhou, T. J. Zwang, G. Hong, Y. Zhao, R. D. Viveros, T.-M. Fu, T. Gao, C. M. Lieber, *Nat. Mater.* **2019**, *18*, 510.
[21] G. A. Woods, N. J. Rommelfanger, G. Hong, *Matter* **2020**, *3*, 1087.
[22] C. Sun, Z. Cheng, J. Abu-Halimah, B. Tian, *iScience* **2023**, *26*, 106715.
[23] T. Wang, M. Wang, J. Wang, L. Yang, X. Ren, G. Song, S. Chen, Y. Yuan, R. Liu, L. Pan, Z. Li, W. R. Leow, Y. Luo, S. Ji, Z. Cui, K. He, F. Zhang, F. Lv, Y. Tian, K. Cai, B. Yang, J. Niu, H. Zou, S. Liu, G. Xu, X. Fan, B. Hu, X. J. Loh, L. Wang, X. Chen, *Nat. Electron.* **2022**, *5*, 586.
[24] P. Gkoupidenis, Y. Zhang, H. Kleemann, H. Ling, F. Santoro, S. Fabiano, A. Salleo, Y. van de Burgt, *Nat. Rev. Mater.* **2024**, *9*, 134.
[25] Y. Fang, L. Meng, A. Prominski, E. N. Schaumann, M. Seebald, B. Tian, *Chem. Soc. Rev.* **2020**, *49*, 7978.
[26] Y. Li, N. Li, N. De Oliveira, S. Wang, *Matter* **2021**, *4*, 1125.
[27] H. Yuk, J. Wu, X. Zhao, *Nat. Rev. Mater.* **2022**, *7*, 935.
[28] D. Ghezzi, M. R. Antognazza, M. Dal Maschio, E. Lanzarini, F. Benfenati, G. Lanzani, *Nat. Commun.* **2011**, *2*, 166.
[29] D. Ghezzi, M. R. Antognazza, R. Maccarone, S. Bellani, E. Lanzarini, N. Martino, M. Mete, G. Pertile, S. Bisti, G. Lanzani, F. Benfenati, *Nat. Photonics* **2013**, *7*, 400.
[30] J. Yi, G. Zou, J. Huang, X. Ren, Q. Tian, Q. Yu, P. Wang, Y. Yuan, W. Tang, C. Wang, L. Liang, Z. Cao, Y. Li, M. Yu, Y. Jiang, F. Zhang, X. Yang, W. Li, X. Wang, Y. Luo, X. J. Loh, G. Li, B. Hu, Z. Liu, H. Gao, X. Chen, *Nature* **2023**, *624*, 295.
[31] H. Yuk, B. Lu, X. Zhao, H. bioelectronics, *Chem. Soc. Rev.* **2019**, *48*, 1642.
[32] Y. Liu, J. Li, S. Song, J. Kang, Y. Tsao, S. Chen, V. Mottini, K. McConnell, W. Xu, Y.-Q. Zheng, J. B.-H. Tok, P. M. George, Z. Bao, *Nat. Biotechnol.* **2020**, *38*, 1031.
[33] X. Wu, H. Peng, *Sci. Bull.* **2019**, *64*, 634.
[34] M. Berggren, E. D. Głowacki, D. T. Simon, E. Stavrinidou, K. Tybrandt, *Chem. Rev.* **2022**, *122*, 4826.
[35] D. T. Simon, E. O. Gabrielsson, K. Tybrandt, M. Berggren, *Chem. Rev.* **2016**, *116*, 13009.
[36] N. Kasthuri, K. J. Hayworth, D. R. Berger, R. L. Schalek, J. A. Conchello, S. Knowles-Barley, D. Lee, A. Vázquez-Reina, V. Kaynig, T. R. Jones, M. Roberts, J. L. Morgan, J. C. Tapia, H. S. Seung, W. G. Roncal, J. T. Vogelstein, R. Burns, D. L. Sussman, C. E. Priebe, H. Pfister, J. W. Lichtman, *Cell* **2015**, *162*, 648.
[37] M. H. Baslow, *Biosemiotics* **2011**, *4*, 39.
[38] J. W. Lovelace, J. Ma, S. Yadav, K. Chhabria, H. Shen, Z. Pang, T. Qi, R. Sehgal, Y. Zhang, T. Bali, T. Vaissiere, S. Tan, Y. Liu, G. Rumbaugh, L. Ye, D. Kleinfeld, C. Stringer, V. Augustine, *Nature* **2023**, *623*, 387.
[39] R. B. Chang, D. E. Strochlic, E. K. Williams, B. D. Umans, S. D. Liberles, *Cell* **2015**, *161*, 622.
[40] W. Z. Zeng, *Science* **2018**, *362*, 464.
[41] E. Ben-Menachem, *Lancet Neurol.* **2002**, *1*, 477.
[42] R. H. Howland, *Curr. Behav. Neurosci. Rep.* **2014**, *1*, 64.
[43] S. Wang, Q. Li, *IET Nanodielectrics* **2018**, *1*, 80.
[44] B. Stadlober, M. Zirkl, M. Irimia-Vladu, *Chem. Soc. Rev.* **2019**, *48*, 1787.
[45] X. Chen, X. Han, Q.-D. Shen, *Adv. Electron. Mater.* **2017**, *3*, 1600460.
[46] F. Wang, X. Zhu, X. Du, *Adv. Funct. Mater.* **2025**, 2500685.
[47] D. A. McCormick, in *From molecules to networks*, (Eds.: J. H. Byrne, R. Heidelberger, M. N. Waxham), Academic Press, Boston **2014**, pp. 351–376.
[48] F. Wang, M. Liu, C. Liu, Q. Zhao, T. Wang, Z. Wang, X. Du, *Sci. Adv.* **2022**, *8*, abp9369.
[49] F. Wang, M. Liu, C. Liu, C. Huang, L. Zhang, A. Cui, Z. Hu, X. Du, *Natl. Sci. Rev.* **2023**, *10*, nwac164.
[50] X. Zhang, C. Zhang, Y. Lin, P. Hu, Y. Shen, K. Wang, S. Meng, Y. Chai, X. Dai, X. Liu, Y. Liu, X. Mo, C. Cao, S. Li, X. Deng, L. Chen, *ACS Nano* **2016**, *10*, 7279.
[51] D. Shi, V. Dhawan, X. T. Cui, *Curr. Opin. Biotechnol.* **2021**, *72*, 54.
[52] A. Prominski, J. Shi, P. Li, J. Yue, Y. Lin, J. Park, B. Tian, M. Y. Rotenberg, *Nat. Mater.* **2022**, *21*, 647.
[53] Y. Huang, Y. Cui, H. Deng, J. Wang, R. Hong, S. Hu, H. Hou, Y. Dong, H. Wang, J. Chen, L. Li, Y. Xie, P. Sun, X. Fu, L. Yin, W. Xiong, S.-H. Shi, M. Luo, S. Wang, X. Li, X. Sheng, *Nat. Biomed. Eng.* **2023**, *7*, 486.
[54] Y. Jiang, X. Li, B. Liu, J. Yi, Y. Fang, F. Shi, X. Gao, E. Sudzilovsky, R. Parameswaran, K. Koehler, V. Nair, J. Yue, K. Guo, Y. Fang, H.-M. Tsai, G. Freyermuth, R. C. S. Wong, C.-M. Kao, C.-T. Chen, A. W. Nicholls, X. Wu, G. M. G. Shepherd, B. Tian, *Nat. Biomed. Eng.* **2018**, *2*, 508.
[55] Y. Jiang, B. Tian, *Nat. Rev. Mater.* **2018**, *3*, 473.
[56] H.-L. Park, H. Kim, D. Lim, H. Zhou, Y.-H. Kim, Y. Lee, S. Park, T.-W. Lee, *Adv. Mater.* **2020**, *32*, 1906899.

[57] F. Liao, Z. Zhou, B. J. Kim, J. Chen, J. Wang, T. Wan, Y. Zhou, A. T. Hoang, C. Wang, J. Kang, J.-H. Ahn, Y. Chai, *Nat. Electron* **2022**, *5*, 84.
[58] D. I. Medagoda, D. Ghezzi, *Commun. Mater.* **2021**, *2*, 111.
[59] T. Kim, J. G. McCall, Y. H. Jung, X. Huang, E. R. Siuda, Y. Li, J. Song, Y. M. Song, H. A. Pao, R.-H. Kim, C. Lu, S. D. Lee, I.-S. Song, G. Shin, R. Al-Hasani, S. Kim, M. P. Tan, Y. Huang, F. G. Omenetto, J. A. Rogers, M. R. Bruchas, *Science* **2013**, *340*, 211.
[60] H.-Y. Zhang, R.-G. Xiong, *Science* **2023**, *381*, 484.
[61] M. Peng, Q. Zhao, A. Chai, Y. Wang, M. Wang, X. Du, *Matter* **2025**, *8*, 101901.
[62] X. Zhu, F. Wang, Q. Zhao, X. Du, *Adv. Funct. Mater.* **2024**, *34*, 2314575.
[63] F. Wang, C. Liu, Z. Dai, W. Xu, X. Ma, Y. Gao, X. Ge, W. Zheng, X. Du, *Innovation* **2025**, *6*, 100742.
[64] C. Liu, F. Wang, X. Du, *Device* **2024**, *2*, 100465.